HHS Public Access

Author manuscript

Dev Cell. Author manuscript; available in PMC 2020 October 07.

Published in final edited form as:

Dev Cell. 2019 October 07; 51(1): 49–61.e4. doi:10.1016/j.devcel.2019.08.005.

Cell size pleomorphism drives aberrant clone dispersal in proliferating epithelia

Subramanian P. Ramanathan[1], **Matej Krajnc**[2], **Matthew C. Gibson**[1,3,4,*]

[1]Stowers Institute for Medical Research, 1000 East 50th Street, Kansas City, Missouri 64110, USA

[2]The Lewis-Sigler Institute for Integrative Genomics, Princeton University, Princeton, NJ 08544, USA

[3]Department of Anatomy and Cell Biology, University of Kansas Medical Center, 3901 Rainbow Boulevard, Kansas City, Kansas 66160, USA

[4]Lead Contact

SUMMARY

As epithelial tissues develop, groups of cells related by descent tend to associate in clonal populations rather than dispersing within the cell layer. While frequently assumed to be a result of differential adhesion, precise mechanisms controlling clonal cohesiveness remain unknown. Here we employ computational simulations to modulate epithelial cell size *in silico* and show that junctions between small cells frequently collapse, resulting in clone cell dispersal amongst larger neighbors. Consistent with similar dynamics *in vivo*, we further demonstrate that mosaic disruption of *Drosophila* Tor generates small cells and results in aberrant clone dispersal in developing wing disc epithelia. We propose a geometric basis for this phenomenon, supported in part by the observation that soap foam cells exhibit similar size-dependent junctional rearrangements. Combined, these results establish a link between cell size pleomorphism and the control of epithelial cell packing, with potential implications for understanding tumor cell dispersal in human disease.

Graphical Abstract

*Correspondence: mg2@stowers.org.

AUTHOR CONTRIBUTIONS

S.P.R and M.C.G designed the project and wrote the manuscript. S.P.R and M.K. performed the experiments and analyzed the data.

DECLARATION OF INTERESTS

The authors declare no competing interests.

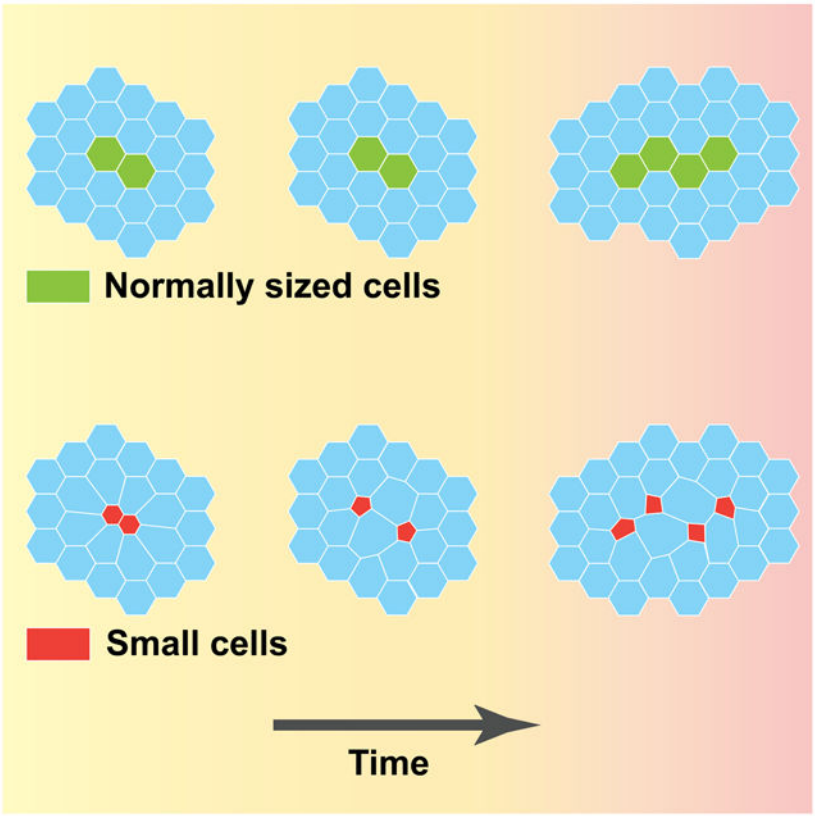

Blurb

Although abnormal cell size variation is one of the defining characteristics of several cancers, the possible role of differential cell size on disease progression is unclear. Ramanathan S. P. et al. discover that the geometric effects of growth heterogeneity can disperse aberrant cells within mosaic epithelial tissue.

INTRODUCTION

Animal tissues are constructed from a mosaic patchwork of genetically divergent clonal cell populations (Lupski, 2013; Freed et al., 2014). Within epithelial tissue, these clones can arise from single progenitors carrying somatic mutations (Lynch, 2010), and numerous human conditions are associated with clonal expansion of single cells carrying deleterious alleles (Forsberg et al., 2017; Lim et al., 2017; Machiela and Chanock, 2017). From this perspective, the morphology and dynamics of epithelial cell clones can influence both organ development and disease progression (Chabab et al., 2016; Kouzak et al., 2013; Rulands et al., 2018; Waclaw et al., 2015). For example, in comparison to single unifocal tumors, the short-range dispersal of clonal tumor cells within planar epithelia is associated with adverse prognoses for patients with carcinomas of the bladder, breast, liver, lung, prostate, thyroid, or urethra (Sidransky et al., 1992; Lutzeyer et al., 1982; Pandis et al., 1995; Weissenbacher et al., 2010; Hsu et al., 1991; Goh et al., 2014; Wang et al., 2009; Marcq and Galy, 1973; Ruijter et al., 1999; Miller and Cygan, 1994; McCarthy et al., 2006; Kim et al., 2008; Hafner

et al., 2001; Corrado et al., 1991). Tremendous effort has been focused on understanding how cells from tumors migrate out of epithelial layers and invade other tissues (Talmadge and Fidler, 2010; Stuelten et al., 2018). In contrast, despite the emerging impact of short-range cell dispersal in development and disease, general principles behind how clonal cells disperse within epithelial tissue are mostly unknown.

Physical forces control cell shape and position within tissue during development as well as during disease (Dreher et al., 2016; Pasakarnis et al., 2016; Hoffman and Crocker, 2009). Indeed, the markedly different mechanical properties of tumor cells when compared to their surroundings have central roles in disease progression (Porta and Zapperi, 2017). In contrast to healthy cells of the same type that typically maintain strikingly uniform size, tumor cells are pleomorphic and can exhibit large variations in shape and size (Ginzberg et al., 2015). Furthermore, abnormal cell size variation serves as a diagnostic criterion for several carcinomas (El-Naggar et al., 2017; Travis et al., 2015). Despite this, the potential role of cell size variance in disease progression remains unclear. In this study, we interrogate the role of cell size discrepancy in tissue organization by inducing clonal populations of small cells within mosaic epithelia.

RESULTS

In silico simulations predict aberrant dispersal of small-cell clones

Organ and clone shape are determined by how populations of individual cells are positioned within a tissue. Existing knowledge of how epithelial cells organize is mostly derived from examining how tension and adhesion determine the stability and topology of cell junctions in populations of comparably sized cells (Fagotto, 2014). To ask how cell size variation might influence tissue organization we first employed a vertex model to simulate a mosaic tissue *in silico* (Figure 1A, B; Farhadifar et al., 2007; Hufnagel et al., 2007; Bi et al., 2015). A single randomly-chosen hexagonal cell from a tissue comprising 20 cells served as the clonal progenitor. After several rounds of cell division, this progenitor gave rise to a largely coherent population related by common lineage (Figure 1C). Next, we induced clonal discrepancies in cell size by altering the preferred surface area of the clone progenitor and its descendants (Figure 1D, Video 1). Contrasting with a general cohesion of control clones after eight rounds of cell division, experimental clones comprised of small cells dispersed 1.7 times more frequently (Figure 1E; cell size reduced by half). Although clonal populations of cells remained contiguous in the initial rounds of cell division, after four rounds of cell cycling, the tendency of clonal cells to disperse strongly depended on cell size (Figure 1F). Interestingly, these rearrangements were associated with topological changes wherein smaller cells consistently lost sides to their immediate neighbors (Figure 1G). In contrast to several non-biological contexts where particles cluster together on the basis of size, these results indicate that clonal epithelial cells should disperse when surrounded by larger neighbors (Anderson and Bunas, 1993; Rosato et al., 1987). The strong correlation between clone contiguity and cell size *in silico* indicates that cell size pleomorphism is sufficient to drive aberrant clone dispersal in vivo.

Aberrant dispersal of small *Tor*$^{\Delta P}$ cells in mosaic *Drosophila* epithelia

To test the biological relationship between cell size and clone contiguity, we next introduced cell size discrepancies *in vivo*, using the *Drosophila melanogaster* wing imaginal disc as a genetically tractable experimental system. We first generated mosaic tissue by perturbing growth in clonal cell populations using Gal4/UAS-mediated gene knockdown (Brand and Perrimon, 1993). Yorkie (Yap/Taz), Myc and Tor are key mediators of cell growth and act downstream of several major cell-signaling pathways (Lloyd, 2013). Their functions as cell growth regulators are conserved across several organisms and tissues, including in the *Drosophila* wing disc (Huang et al., 2005; Johnston et al., 1999; Saucedo et al., 2003). In keeping with the results of our *in silico* studies, clonal populations of cells expressing *Myc* and *Tor RNAi* exhibited reduced size and often lost junctional contact with each other and dispersed among their *wild-type* neighbors (Figure S1A-D, Table S1). We decided to investigate the influence of size control in epithelial cell mixing by focusing on the Tor pathway for two reasons: (1) In contrast to *Tor*, clonal disruption of *Yorkie* or *Myc* triggers extensive confounding pleiotropic effects on epithelial cell dynamics, including apoptosis and aberrant junction tension (Bosveld et al., 2016; Di Gregorio et al., 2016; Levayer et al., 2015); (2) *Tor-RNAi* expressing cells dispersed more frequently than those expressing *Yorkie*- or *Myc-RNAi* (Figure S1E).

To confirm the Tor-dependent dispersal phenotype from RNAi experiments, we next employed the MARCM technique (Lee and Luo, 1999) to generate cell clones homozygous for the null allele *Tor*$^{\Delta P}$ in developing wing discs (Figure 2A, B; Zhang et al., 2000). We first quantified the effect of *Tor* loss on cell volume and apical surface area. Estimating volumes of interphase epithelial cells is challenging due to both cell-cycle dependent fluctuations in volume as well as their irregular three-dimensional shape (Gómez-Gálvez et al., 2018). In contrast, most animal cells maintain a roughly spherical shape during mitosis (Meyer et al., 2011; Nakajima et al., 2013; Ramanathan et al., 2015). By measuring mitotic cell size, we were able to overcome both spatial and temporal challenges (Figure S2A-G). We estimated cell volume by measuring mitotic spherical cross-sectional cell area and found that *Tor*$^{\Delta P}$ cells were 50.8 ± 2.7% (mean ± s.e.m.) the volume of neighboring cells in the developing wing pouch (Figure S2H, I). During interphase, for an elongated epithelial cell of constant height, a 50% reduction in volume would correspond to ~50% reduction in the average cross-sectional area. We therefore skeletonized images of epithelial junctions and extracted the interphase cell shape parameters using EpiTools (Figure 2C, D) (Heller et al., 2016). In agreement with our geometric prediction, the apical areas of interphase *Tor*$^{\Delta P}$ cells were reduced by 55.3 ± 1.4% in comparison to their immediate neighbors in the wing pouch (Figure 2E). This suggests that the smaller apical area of *Tor*$^{\Delta P}$ cells is a consequence of growth perturbation.

Having quantified the growth defect in the volume and apical surface area of *Tor*$^{\Delta P}$ cells, we next investigated corresponding abnormalities in clone contiguity. In agreement with the observation of aberrant cell dispersal in *Act>>Gal4, UAS-Tor RNAi* clones, *Tor*$^{\Delta P}$ cells were extensively intervened by their non-clonal neighbors and more dispersed than controls (Figure 2B, F). Frequently, *Tor*$^{\Delta P}$ cells were separated at apico-lateral regions of the epithelia while still maintaining contact at the apical-most junctions in three-dimensional

reconstructions (Video 2, 3). This suggests a limited role for apical cytoskeletal and adhesion molecules in driving the dispersal of $Tor^{\Delta P}$ cells. Clonal cells related by lineage are almost always contiguous in wing disc epithelia (Resino et al., 2002). Contrary to expectations, and in agreement with the simulations *in silico*, introducing cell size discrepancy by inducing $Tor^{\Delta p}$ clones allowed larger neighbors to intermix with clonal cells. These results show that cell size discrepancies can influence how cells are positioned within mosaic epithelial tissue *in vivo*.

Small $Tor^{\Delta P}$ cells disperse by losing sides to larger neighbors

Statistical descriptions of how cells are packed in plants, animals and even soap-foam report a positive correlation between cell sidedness and apical cell area, generally known as Lewis' Law (Lewis, 1928; Hilgenfeldt, 2013; Durand et al., 2014). In contrast to plant epidermis, however, epithelial cell junctions are amenable to topological rearrangements accompanying cellular growth and proliferation. We therefore examined how cell size discrepancies influence local epithelial topology in the wing disc (Figure 2C, D). Under steady state conditions, a majority of wing disc cells are six-sided and three-sided cells are notably absent (Gibson et al., 2006; Heller et al., 2016). Interestingly, $Tor^{\Delta P}$ clones exhibited three-sided cells at a non-zero frequency of 2.4% (Figure 2D). Furthermore, a majority of $Tor^{\Delta P}$ cells had five instead of the expected six sides (exhibiting an average neighbor number of 5.25 ± 0.10 versus 6.12 ± 0.03 calculated in controls; Figure 2G). Cellular movements in epithelia often occur through neighbor exchanges driven by cell-junction rearrangements (Walck-Shannon and Hardin, 2014). We therefore investigated whether $Tor^{\Delta P}$ cells lose sides and intercalate with neighbors because the shared junctions between $Tor^{\Delta P}$ cells are unstable (Figure 2D, G). To dissect the dynamics of how the $Tor^{\Delta P}$ cells lose sides, we quantified the sidedness of clonal cells and their immediate neighbors (Figure 3A). In agreement with previous studies on epithelial topology, the average sidedness of control clones and their primary and secondary neighbors was 6.11 ± 0.01, 6.01 ± 0.02 and 6.04 ± 0.03, respectively (Figure 3A) (Gibson et al., 2006). Interestingly, not only did clonal $Tor^{\Delta P}$ cells tend to lose sides, but their primary neighbors also tended to gain sides, featuring an average sidedness of 6.56 ± 0.02 (Figure 3B). The secondary neighbors exhibited an average sidedness of 5.97 ± 0.01, suggesting that cell size discrepancies drive highly localized topological rearrangements. In agreement with our *in vivo* analysis, clone cell dispersal *in silico* was associated with smaller cells losing sides and their normally-sided immediate neighbors gaining sides (Figure 1G).

To directly confirm the role of cell size in cell rearrangement we performed live imaging in developing wing discs. Time-lapse imaging showed that $Tor^{\Delta P}$ cells consistently lost sides to their larger neighbors and separated from each other during interphase, rather than mitosis (Video 4). This indicates that junctions between $Tor^{\Delta P}$ cells were established post-mitotically, but later became unstable and collapsed. Combined, these findings allow us to postulate that cell size pleomorphism can influence local epithelial topology, and that junction instability between small cells can disperse epithelial clones.

A prominent role for the TORC1 complex in *Tor*-mediated cell rearrangement

The two protein complexes formed by Tor, known as Tor complex 1 (TORC1) and Tor complex 2 (TORC2), perform distinct biological functions. While TORC1 controls cell size by modulating metabolism, TORC2 regulates more diverse cellular functions, including the actin cytoskeleton (Saxton and Sabatini, 2017). Changes to the actin cytoskeleton can influence epithelial remodeling (Bertet et al., 2004; Martin et al., 2009; Rauzi et al., 2010), therefore we sought to distinguish between the roles of TORC1 and TORC2 in modulating epithelial topology. RheB is an upstream activator of the TORC1 pathway but is dispensable for TORC2 activity (Yang et al., 2006a). Conversely, Lst8 and Sin1 are essential components of TORC2, but are not necessary for TORC1 function (Wang et al., 2012; Yang et al., 2006b). Using the MARCM technique, we induced clones carrying homozygous loss-of-function alleles for $RheB^{2d1}$, $Lst8^{1}$ or $Sin1^{e3756}$ (Figure S3A, B). $RheB^{2d}$ cells frequently lost junctional contact with one another and were interposed by non-clonal neighbors. In agreement with our observations with $Tor^{\Delta P}$ clones, during instances of $RheB^{2d1}$ clone dispersal, the size disparity between mutant cells and their larger non-clonal neighbors was visually apparent (Figure 3A).

Consistent with a negligible role for TORC2 activity in clone dispersal, $Lst8^{1}$ and $Sin1^{e3756}$ clones stayed contiguous (Figure S3B). In *Drosophila*, the enrichment of F-actin and myosin in the vicinity of cell junctions can induce their shrinkage and thereby drive cell intercalation (Munjal and Lecuit, 2014). We therefore examined the actin cytoskeleton at junctions shared between $Tor^{\Delta P}$ cells. Compared to surrounding tissue, junctions shared by $Tor^{\Delta P}$ cells did not preferentially enrich components of the actin cytoskeleton (F-actin and p-myosin, Figure S3C, D). These experiments do not support a causal role for changes in the actin cytoskeleton in $Tor^{\Delta P}$ clone dispersal. This interpretation is further supported by experiments showing that clonal cell populations disperse as a result of perturbing TORC1 and not TORC2.

Ectopic E-cadherin fails to rescue $Tor^{\Delta P}$ clone dispersal

Cadherins are transmembrane proteins that mechanically link adjacent cells and are essential for epithelial cell cohesion (Lecuit and Yap, 2015). Indeed, disrupting E-cadherin can destabilize cell junctions and induce cell motility during development and in disease (Cavallaro et al., 2002; Gumbiner, 2005). As the Tor pathway regulates protein synthesis, we investigated whether $Tor^{\Delta P}$ cells might disperse due to reduced junctional E-cadherin. However, levels of both E-cadherin and its cytoskeletal linker β-catenin were unaffected in $Tor^{\Delta P}$ cells (Figure S3E, F). E-cadherin-mediated adhesion is further dependent on stable homophilic interactions at cell-cell junctions (Lecuit and Yap, 2015). Although junctional E-cadherin was not reduced, we investigated whether its stability was perturbed in $Tor^{\Delta P}$ cells. To test this, we induced $Tor^{\Delta P}$ clones in tissue expressing endogenous *Drosophila* E-cadherin fused to tdTomato (Figure 4A) (Huang et al., 2009). We then photobleached small regions of junctional E-cad$^{\text{Tomato}}$ and allowed fluorescence to recover (Figure 4B) (Cavey et al., 2008; Erami et al., 2016). Prior to photobleaching, junctional levels of E-cad$^{\text{Tomato}}$ were comparable between clonal $Tor^{\Delta P}$ cells (C:C, 1.7 ± 0.2), non-clonal cells (N:N, 1.7 ± 0.1) and between nonclonal and $Tor^{\Delta P}$ cells (C:N, 1.5 ± 0.1) (Figure 4C). After photobleaching, junctional E-cad$^{\text{Tomato}}$ failed to recover to prebleach levels and converged to nearly identical

final intensities regardless of cell genotype (C:C, 1.1 ± 0.1; N:N, 1.1 ± 0.1 and C:N, 1.0 ± 0.1). This is indicative of identical mobile, and likely monomeric, junctional E-cad^{Tomato} concentrations across the three junction types. Furthermore, the immobile fractions across the three junction types were also similar (C:C, 0.58 ± 0.09; N:N, 0.54 ± 0.06 and C:N, 0.52 ± 0.07) (Figure 4D). This is indicative of identical stable, and likely extracellularly-interacting junctional E-cad^{Tomato} concentrations across the three junction types. These results are in agreement with previous reports showing over 50% of the junctional E-cadherin to be immobile, and therefore able to stabilize cell-junctions (Yamada et al., 2005; Cavey et al., 2008; Erami et al., 2016). To further investigate the dependency between *Tor*$^{\Delta P}$ cell dispersal and cell-adhesion, we clonally overexpressed *Drosophila* E-cadherin (Figure 4E, F). Interestingly, increasing junctional E-cadherin in *Tor*$^{\Delta P}$ clones did not prevent them from dispersing extensively (Figure 4F, G). Altogether, these results suggest that *Tor*$^{\Delta P}$ clone dispersal is due factors other than altered cell adhesion.

Tor$^{\Delta P}$-mediated cell rearrangement is not due to apoptosis

Apoptosis can have a profound effect on local topology and tissue reorganization through several means, including triggering directed cell division, regulating differential actomyosin activation, or even through inducing packing defects (Monier et al., 2015; Li et al., 2009; Levayer et al., 2015; Saw et al., 2017; Tsuboi et al., 2018). The influence of Tor in apoptosis is context-dependent, as Tor inhibition is associated with both increased and decreased apoptosis (Wang and Edgar, 2010). We thus investigated whether apoptosis plays a role in *Tor*$^{\Delta P}$-mediated cell rearrangement in mosaic wing disc epithelia. To determine if cell death was prevalent in *Tor*$^{\Delta P}$ clones, we stained for the apoptotic marker, cleaved *Drosophila* Dcp1, and did not observe any instance of cell death within *Tor*$^{\Delta P}$ clones in the third instar wing disc (Figure 5A, B). Although inducing *Tor*$^{\Delta P}$ clones did not increase the frequency of apoptosis in the final stages of wing disc development, we asked if apoptosis was required to disperse cells in the earlier stages of *Tor*$^{\Delta P}$ clone morphogenesis. Overexpressing the caspase inhibitor, p35, to block apoptosis in *Tor*$^{\Delta P}$ clones did not prevent their dispersal (Figure 5C, D). These experiments show that apoptosis is neither prevalent in clonal *Tor*$^{\Delta P}$ cells nor essential for their dispersal in mosaic epithelia.

Slower cell proliferation is not sufficient to destabilize clonal junctions

Perturbing major growth regulators, including Yorkie (Yap/Taz), Myc, or Tor can also influence cell proliferation rate through diverse mechanisms (Huang et al., 2005; Johnston et al., 1999; Morita et al., 2015). We therefore sought to test the role of cell proliferation rate on aberrant clone dispersal. Rbf is a negative regulator of the transcription factor E2F and its overexpression prolongs all the phases of cell cycle (Neufeld et al., 1998). To determine if discrepancies in cell proliferation rates destabilize cell junctions in general, we disrupted the cell cycle by co-expressing *Rbf* and *p35* in clonal cell populations using the Gal4/UAS system (Figure S4 A, B). In agreement with previous observations, the cell cycle duration of *Rbf*-overexpressing clonal cell populations almost doubled (20.7 ± 2.7 h vs 10.6 ± 0.3 h for controls; Figure S4 C-E). Nevertheless, slow-cycling *Rbf* overexpressing cells did not exhibit reduce apical cell areas, dispersal among their neighbors, or a tendency to lose sides (Figure S4 F-J). These results suggest that reduced proliferation rates are not sufficient to destabilize cell junctions and disperse clonal cells.

Changing sidedness: a geometric basis for clone separation

Our experiments, both *in silico* and *in vivo*, suggest that $Tor^{\Delta P}$ cell junction instability is not directly induced by differences in cell adhesion, contractility or apoptosis. This led us to consider a geometric basis for size discrepancy-induced junction rearrangements. Irrespective of cell size, the side lengths of abutting cells have to be equal in contiguous epithelia. We asked how this fundamental topological requirement is satisfied in $Tor^{\Delta P}$ mosaic tissue. Regular polygons with different areas have correspondingly mismatched side-lengths (Figure S5A). As fixed area polygons become more anisotropic, their perimeters and hence their average side lengths will increase (Figure S5B). We first asked if the smaller $Tor^{\Delta P}$ cell and their neighbors match side lengths by changing cell anisotropy. In the wing pouch, control clone cells and their primary neighbors showed a similar degree of anisotropy (Figure S5C). The average $Tor^{\Delta P}$ cell aspect ratio (1.53 ± 0.02) was nearly identical to immediate neighbors (1.52 ± 0.01) as well to FRT40A controls (1.52 ± 0.01; Figure S5D, E). This indicates that changes in cell anisotropy to match neighbor cell side lengths were limited.

Clonal cell dispersal was associated with a loss of $Tor^{\Delta P}$ cell sidedness and a concomitant gain in neighbor cell sidedness (Figure 3). For a regular polygon of fixed area, reducing the number of sides will necessarily increase the average length of those that remain. Conversely, increasing the number of sides will reduce the average side-length (Figure 6A, B, C). We hypothesized that conflicts between the preferred side lengths of epithelial polygons of different size could result in local topological rearrangements (Figure 6D). The area of an isotropic polygon scales with the square of its length. Therefore, we grouped $Tor^{\Delta P}$ cells and their neighbors by polygon class and fit their side-lengths and areas to a square root function. Despite the wide distribution of cell lengths and areas, the fits for $Tor^{\Delta P}$ cells, their neighbors and for control clone cells were strikingly similar within a polygon class (Figure S6, Table S2). These results indicate that side lengths of $Tor^{\Delta P}$ cells would be indistinguishable from *wild-type* cells of similar size, despite the genetic perturbation. Furthermore, in agreement with the geometric arguments above, for a given cell size both $Tor^{\Delta P}$ cells and their neighbors tended to increase side-length upon losing sidedness and *vice versa* (Figure 6C, E). As a consequence of their smaller size, the mean perimeter of $Tor^{\Delta P}$ cells was approximately 28% reduced compared to their primary neighbors (Figure 6F). Nevertheless, because $Tor^{\Delta P}$ cells had fewer sides, their average side-length was within 10% of primary neighbors and their length distributions were still similar despite the cell size differential (Figure 6G, H). Combined, these findings suggest that the conflict between the preferred side length of adjacent cells can induce junction rearrangements.

The results above suggest that small-cell separation in the wing disc has a geometric basis. To test the generality of our observations, we asked if this phenomenon can be observed in non-living cellular systems. Due to their simplicity and similarities with epithelial tissue, soap foam studies provided several early insights into the mechanisms driving planar cell rearrangements (Weaire and Rivier, 1984; Guirao and Bellaïche, 2017; Graner and Riveline, 2017). Interestingly, as with epithelial cells and *in silico* simulations, we observed that small-cell junctions in coarsening soap cells are also frequently unstable causing

neighboring large cells to intervene between two smaller cells (Video 5). The prevalence of small-cell junction instability *in* silico and in soap foam underscores the generality of rearrangement on the basis of cell size in both living and non-living cellular materials.

Tor$^{\Delta P}$ clones disperse due to differential cell size

We postulate that *Tor*$^{\Delta P}$ clone dispersal is due to localized junction rearrangements driven by cell size discrepancy with their neighbors. If this is indeed the case, then restoring *Tor*$^{\Delta P}$ cell size should reduce clone dispersal. S6 kinase is a key downstream target of the TORC1 pathway, and controls cell size by regulating protein synthesis without influencing proliferation rate (Montagne et al., 1999; Oldham et al., 2000). To rescue cell size in *Tor*$^{\Delta P}$ clones, we expressed a constitutively active form of S6 Kinase (S6K^{CA}) (Figure 7A) (Barcelo and Stewart, 2002). *Tor*$^{\Delta P}$ cells were 44.14 ± 1.49 % the area of their primary neighbors (Figure 7B). Expressing *S6K*^{CA} in *Tor*$^{\Delta P}$ clones restored apical cell area to 88.73 ± 3.76 % of their neighboring cells (Figure 7B). Correspondingly, the rescued mutant clone cells increased sidedness to 5.87 ± 0.04 and exhibited reduced dispersal (Figure 7A, C). In agreement with the previous reports, *Tor*$^{\Delta P}$ cell cycle duration increased to 14.3 ± 0.9 h compared to 10.3 ± 0.5 h in controls (Figure 7D) (Morita et al., 2015; Zhang et al., 2000). Interestingly, expressing *S6K*^{CA} in controls did not change their cycle duration (10.6 ± 0.4 h). Furthermore, the cell cycle of *Tor*$^{\Delta P}$+S6K^{CA} cells (12.4 ± 0.4 h) was significantly longer than the controls and was not different from that of *Tor*$^{\Delta P}$ cells (Figure 7D). The fact that *S6K*^{CA} expression rescued *Tor*$^{\Delta P}$ cell area and clone contiguity without restoring cell cycle duration indicates that differential proliferation rates did not cause *Tor*$^{\Delta P}$ clone dispersal. Expressing Tor in a *Tor*$^{\Delta P}$ background only partially restores growth and development in *Drosophila* (Hennig and Neufeld, 2002). Indeed, upon overexpressing *Tor, Tor*$^{\Delta P}$ MARCM clones exhibited a varying degree of cell area rescue (Figure 7E). Nevertheless, restoration of cell sidedness and clone contiguity still correlated closely with the extent of cell area rescue (Figure 7E, F). Altogether, these results confirm that reducing cell size alone can indeed influence local topology and clone contiguity.

We next sought to distinguish between the role of relative versus absolute cell size in dispersing *Tor*$^{\Delta P}$ clones. *Minute* mutations are a group of lesions defective in ribosomal protein production and associated with dominant developmental defects, including slower cell growth and proliferation in *Drosophila* (Lambertsson, 1998). We first generated *wild-type* clones surrounded by a slow-growing heterozygous population of *Minute* neighbors which were 22.94% smaller than the *wild-type* cells (Figure S7A-C). Consistent with a role for cell size in cell topology, *Minute* cells immediately adjacent to the clone had only 5.87 ± 0.03 sides while the clone cells had a slightly increased average sidedness of 6.23 ± 0.04 sides (Figure S7D). Interestingly, these results are in agreement with those predicted *in silico*, where larger clonal cells tended to gain sides in mosaic tissue (Figure 1G). These results also agree with previous reports that show *wild-type* clones can intermix with surrounding heterozygous *Minute* cells (Figure S7A, E) (Li et al., 2009; Simpson, 1979). We then generated small *Tor*$^{\Delta P}$ cells surrounded by *Minute* neighbors (Figure S7B). Surrounding *Tor*$^{\Delta P}$ cells with growth deficient *Minute* cells decreased the clone-neighbor area discrepancy to 69.50 ± 3.82% (compared with 44.7 ± 1.4 when surrounded by normally-sized neighbors; Figures 7F). This reduction in size discrepancy correlated with a

restoration of the mean sidedness of $Tor^{\Delta P}$ cells to 5.77 ± 0.04, and reduced their mixing with neighbors (Figure 7E, F). In sum, these observations indicate that relative, rather than absolute, cell size variation induces local cell intercalation and disperse clonal cell populations within epithelial tissue.

DISCUSSION

Planar cell rearrangement is a major driver of animal tissue morphogenesis. By controlling cell junction stability, the apical actomyosin and adhesion machineries modulate cell-neighbor exchanges (Bertet et al., 2004; Martin et al., 2009; Rauzi et al., 2010). Nevertheless, recent studies showing neighbor exchanges can initiate at the lateral and basal regions of epithelia suggest there are biological and mechanical aspects of cell intercalation which remain to be explored (Williams et al., 2014; Sun et al., 2017; Gómez-Gálvez et al., 2018). Previous studies have noted that perturbing the cellular growth regulators Myc and Minutes can induce epithelial cell mixing (Levayer et al., 2015; Li et al., 2009). Cell mixing in these contexts was attributed to junctional F-actin enrichment and aberrant planar polarity triggered by apoptosis. Our results *in silico* and *in vivo* show that growth deficient clonal cells disperse due to cell size discrepancies. Dispersal of $Tor^{\Delta P}$ clones emerged as an unexpected consequence local topological rearrangement due to an instability of the junctions between small cells (Figure 6). Reducing the size discrepancy between $Tor^{\Delta P}$ cell size and their neighbors restored both cell sidedness and clone contiguity (Figure 7). In contrast to Myc and Minutes, apoptosis was not prevalent in $Tor^{\Delta P}$ clones (Figure 5). Furthermore, we conclude that junction instability in $Tor^{\Delta P}$ clones is not the result of elevated tension between small-cell junctions based on the following three observations: (1) Small cell clones disperse in computational simulations with uniform edge tensions (Figure 1F); (2) Immunostaining wing discs containing $Tor^{\Delta P}$ clones did not show increased actomyosin localization between $Tor^{\Delta P}$ cell junctions (Figure S4); (3) Elevated tension is predicted to shorten cell-junctions (Bertet et al., 2004; Rauzi et al., 2010; Bardet et al., 2013). Nevertheless, the side lengths of the smaller cells were still comparable to their neighbors (Figure 6H). Our results also suggest that small-cell dispersal driven by geometric constraints may not be restricted to the apical plane of the epithelium and can occur at any plane along the length of an epithelium where there is cross-sectional cell area discrepancy (Video 3, Figure 6C, D). Interestingly, cell area changes precede junction fluctuations during germ band extension in *Drosophila* (Vanderleest et al., 2018). Based on this, it is tempting to contemplate a role for cell size in epithelial intercalation in developmental contexts as well.

Although a positive correlation between cell sidedness and cell area was first noted in both plant and animal tissue by Lewis' pioneering work in 1928, the capacity for cell size changes to drive topological rearrangements has not been previously proposed. We find that reducing cell size within a clonal population triggers rearrangement of local topology such that larger cells gain sides at the expense of smaller cells (Figure 3C and Video 4). This transformation allows the abutting cells to match side-lengths and still maintain shape isotropy (Figure 6H). Interestingly, in plant epidermis, where junction rearrangements are absent, cells match side lengths by increasing anisotropy (Kim et al., 2014). Increasing shape anisotropy, and thus, cell perimeter, may not be energetically favorable in epithelial cells with tensile junctions (Figure S5). These results reveal important distinctions in the

rules employed to pack plant and animal cells into tissue. As observed in animal epithelial cells, coarsening soap cells also exhibit small-cell junction instability and subsequent cell separation (Video 5). In this regard, junction instability driven by cell size discrepancies could be a feature of diverse tensile topological systems.

Cell size heterogeneity is one of the earliest hallmarks of cancer development (El-Naggar et al., 2017; Ginzberg et al., 2015; Travis et al., 2015). Indeed, several key determinants of cell size including ploidy and the regulation of cellular metabolism are commonly disrupted in tumors (Schmoller and Skotheim, 2015). Although growth-deficient small cell clones disperse, the influence of aberrant ploidy on clone contiguity remains to be tested. Interestingly, discrepancies in either protein synthesis or ploidy are poorly tolerated in mosaic epithelia and competitive elimination of such 'less-fit' smaller cells from tissue can promote fitness (Di Gregorio et al., 2016; Merino et al., 2015). On the other hand, given that the Tor pathway is misregulated in several diseases, how $Tor^{\Delta P}$ clones evade competitive processes is an important avenue for further investigation (Di Gregorio et al., 2016; Saxton and Sabatini, 2017). The dispersal of the tumor cells within the epithelium is indicative of adverse prognosis in several carcinomas (Lutzeyer et al., 1982; Weissenbacher et al., 2010; Goh et al., 2014; Marcq and Galy, 1973; Miller and Cygan, 1994; Kim et al., 2008; Corrado et al., 1991). Therefore, understanding both pleomorphism and clonal dispersal during disease progression could be an important direction for future research.

STAR METHODS

Lead Contact and Materials Availability

Further information and requests for resources and reagents should be directed to and will be fulfilled by the Lead Contact, Matthew C. Gibson (mg2@stowers.org).

Experimental Models and Subject Details

In-silico model

Vertex dynamics.: In the vertex model, a tissue is described as a confluent planar tiling of polygonal cells. Cell shape is parametrized by the positions of vertices $\boldsymbol{r}_v = (x_v, y_v)$, for $v = 1, \ldots N$, where N is the total number of vertices in the system. Cell deformations and movements are described implicitly by the vertex dynamics given by the overdamped equation of motion, which reads

$$\frac{\mathrm{d}\boldsymbol{r}_v}{\mathrm{d}t} = \mu_v \boldsymbol{F}_v, \tag{1}$$

where μ_v is the mobility of vertex v, i.e. the inverse friction drag coefficient. The forces at vertices $\boldsymbol{F}_v$ are assumed conservative and drive the system towards the closest local minimum of the potential energy

$$W = \gamma \sum_{\text{sides } i} l_i + k \sum_{\text{cells } j} (A_j - a_j)^2 . \tag{2}$$

Here l_i and γ are the length of the edge, i.e. cell-cell junction, and the line tension, respectively, A_j and a_j are the actual and the preferred surface area of cell j, whereas k is the cell-compressibility modulus. The force at vertex v is calculated as $\boldsymbol{F}_v = \nabla_v W$, where $\nabla_v = (\partial/\partial x_v, \partial/\partial y_v, \partial/\partial z_v)$. Choosing the average cell surface area of "normal" cells A_0 for the unit area and $A_0^{1/2}$ for the unit length, we rescale the cell-geometry-related variables as: $\boldsymbol{r}_v/A_0^{1/2} \rightarrow \boldsymbol{r}_v$, $l_i/A_0^{1/2} \rightarrow l_i$, $A_j/A_0 \rightarrow A_j$, and $a_j/A_0 \rightarrow a_j$. Furthermore, assuming that all vertices have the same mobility ($\mu_v = \mu$ for all v), the characteristic time $\tau = A_0^{1/2}(\gamma\mu)^{-1}$. In dimensionless form, the equation of motion for vertex v reads

$$\frac{\mathrm{d}\boldsymbol{r}_v}{\mathrm{d}t} = -\sum_{\text{sides } i} \nabla_v l_i - 2\kappa \sum_{\text{cells } j} (A_j - a_j)\nabla_v A_j, \tag{3}$$

where $\kappa = kA_0^{3/2}/\gamma$ is the dimensionless cell-compressibility modulus. Here we assume that cells are almost incompressible and we set $\kappa = 100$. Equation (3) is solved using a forward finite-difference scheme with time step $\Delta t = 10^{-4}$.

Growth.: We assume a simple cell-growth model, in which cells are inactive during their *rest phase* and undergo linear area growth during the *growth phase*. In particular, the preferred area of cell j increases linearly during the growth phase as $a_j(t) = a_j[1 + (1/\tau_j)(t - t_j^{(0)})]$, where a_j is the preferred area of cell j in the rest phase, τ_j is the duration of the growth phase, whereas $t_j^{(0)}$ is the time at which cell enters the growth phase. Both τ_j and the duration of the rest phase T_j are random variables: $T_j = T_0 + \xi(\sigma_T)$ and $\tau_j = \tau_0 + \xi(\sigma_\tau)$, where $\xi(\sigma)$ is a Normally distributed random variable, whereas T_0 and τ_0 are the average duration of the rest and the growth phase, respectively. In our simulations $T_0 = 50$, $\tau_0 = 2$, $\sigma_T = 2$, and $\sigma_\tau = 0.2$. Cell divides when A_j reaches double the rest-phase preferred area ($2a_j$).

Boundary conditions.: The simulations are performed in a square domain of size $L \times L$ with periodic boundary conditions. Since cells are almost incompressible, we can assume that the total surface area of the tissue at any given time equals the sum of the preferred surface areas of individual cells. Additionally, assuming an isotropic growth, i.e. the direction of the cleavage plane is random, at any given time, the linear dimension of the tissue $L(t) = \sum_{\text{cells } j} a_j(t)$.

Initial configuration.: To prepare a random tissue sample, we initially pack 20 cells in a honeycomb lattice and apply periodic boundary conditions on the simulation-box walls. Next, we integrate the equation of motion [Eq. (3)] at fixed number of cells and fixed preferred cell areas while performing T1 transformations on random cell-cell junctions as described in Krajnc et al., 2018. As soon as only half of the cells remain hexagons, we randomly choose a hexagonal cell and change its preferred area to that of the clone cells.

In vivo model

***Drosophila* husbandry and mosaic generation.:** Animals were raised on standard molasses based medium at 25°C and 50% humidity at a 12 hour light/dark cycle. In all experiments, we studied both male and female *Drosophila melanogaster larvae*. To induce clones, wing

discs were heat-shocked for one hour at 37°C, 72 hours prior to dissection, unless otherwise mentioned.

Method Details

Wing disc immunostaining and imaging.—Wing discs of wandering 3rd instar *Drosophila* larvae were dissected in 1× PBS and fixed in 4% Paraformaldehyde for 30 minutes at room temperature. The samples were washed 4× times with PBT (1× PBS with 0.1% TritonX-100) over 1.5 hours. The discs were incubated with primary antibody in PBT over 12 hours at 4°C on a rocker. The samples were then washed 4× times with PBT over 1.5 hours. The samples were incubated with secondary antibody in PBT for 3 hours in room temperature and washed 4× times with PBT over 1.5 hours. To stain for F-actin, the samples were treated with SiR-Jasplakinolide (1:200) in PBT. The samples were mounted in SlowFade Diamond Antifade. For live imaging wing discs, clones were induced later than for fixed imaging by heat-shocking for one hour at 37°C, 48 hours prior to dissection. The wing discs were dissected and imaged in Schneider's medium supplemented with 6.2 μg/ml bovine insulin, 5% fly extract and 1% Pen-Strep. A Leica SP5 confocal using 40× and 63× objectives was used for image acquisition.

Following dilutions were used for the antibodies:

Antibody	Dilution
Mouse anti-*Drosophila* discs large	1:1000
Rabbit anti-*Drosophila* Cleaved Dcp-1 (Asp216)	1:200
Rat anti-*Drosophila* DE-cadherin	1:50
Mouse anti-*Drosophila* β-catenin	1:200
Rabbit anti-human Phospho-Myosin Light Chain 2 (Ser19)	1:50
Goat anti-mouse Alexa Fluor 647	1:500
Goat anti-Rabbit Alexa Fluor 647	1:500
Goat anti-Rat Alexa Fluor 647	1:500
Goat anti-Mouse 405	1:500
Goat anti Rabbit 405	1:500

Image Processing.—To visualize and analyze the topology of the whole curved wing pouch region we used EpiTools to perform selective plane projection that follows the curvature of the whole tissue (Heller D. et al., 2016). Adjustments to image contrast, brightness and size were performed by linear interpolation and applied to the whole image using FIJI. Drift correction in time-lapse images was performed using StackReg FIJI plugin. To visualize the localization of cytoskeletal molecules we performed Z-projections on image stacks using FIJI. Images were compiled with Adobe Illustrator CC.

FRAP experiments.—The wing discs were dissected and imaged in Schneider's medium supplemented with 6.2 μg/ml bovine insulin, 5% fly extract and 1% Pen-Strep. A Leica SP5 confocal using 63×, 1.2 NA water objective was used for photobleaching and image

acquisition. Pinhole size was two airy units and averaging was from two line-scans. The image size was 256×256 pixels with a resolution of 0.10 μm/pixel acquired at scan zoom 10× and scan speed 700. Clonal cells were identified by imaging $mCD8^{GFP}$ and $E\text{-}cad^{Tomato}$ with 458 nm and 561 nm excitation. Subsequent pre- and post-bleach images were acquired with only 561 nm excitation. Post-bleach images were acquired every 10 s for at least 120 s. Photobleaching was performed by scanning circular regions of interest (ROIs) of one-micron diameter with 561 nm laser at 100% power. In every FRAP experiment, we simultaneously photobleached three junctions shared between nonclonal, clonal-nonclonal or clonal cells. Samples drifting out of the focal plane were excluded from further analysis. Drift within the focal plane was corrected manually with FIJI. Junctional $E\text{-}cad^{Tomato}$ enrichment is the mean pixel intensity of an ROI normalized to mean pixel intensity of the entire field of view. The recovery of junctional $E\text{-}cad^{Tomato}$ enrichments were fit to an exponential function $y(t) = a \times (1 - e^{-bt}) + c$, as described previously (Erami et al., 2016). The immobile fractions were determined as $F_{im} = 1 - [a/(I_p - c)]$ using the prebleach junctional $E\text{-}cad^{Tomato}$ enrichment I_p and the parameters derived from the exponential fit.

2-D foam.—Soap bubbles were generated by agitating ~20% dishwashing liquid in water. The bubbles were transferred to a black colored plastic substrate. Two 0.75 mm thick glass micro coverslip served as spacers. A 25×75 mm glass microscope slide resting on the two spacers confined the bubbles to generate 2-D foam. The coarsening soap cells were imaged using a web camera.

Quantification and Statistical Analysis

Quantification.—Cell position, sidedness, and area within the wing disc pouch region were visualized and quantified by first generating the skeletonized image of the wing disc junctions. Icy (F. de Chaumont, S et al., 2012) and EpiTools package for Icy (Heller D. et al., 2016) were used export data from the skeletonized images. Cells with a number of sides less than three and greater than nine were regarded as outliers and not included in subsequent analysis. Only clonal cells abutting GFP-negative cells were considered for determining clone cell sidedness and apical cell area. Relative cell area was obtained by normalizing with the respective mean area of the 1^0 neighbors for each wing disc. Relative cell side-length was determined by normalizing with the respective square root of the mean area of the 1^0 neighbors for each wing disc. The total number of clonal cells in the wing pouch was quantified manually using the multi-point tool in FIJI. Cells scatter of clones in a wing disc is the number of times GFP+ cells that are separated by one GFP-negative cell. A time point 8 minutes prior to cytokinesis was used for determining mitotic cross-sectional area from Z-projections. Relative mitotic areas were determined by normalizing with mitotic control neighbors. For a proliferating tissue where apoptosis is uncommon, the average cell cycle duration $T_{Cycle} = t_{Clone}/log_2 (n_{Clone}/N_{Control})$. Here, t_{Clone} is the time interval between the induction of single GFP+ progenitors in the wing pouch until they are fixed with paraformaldehyde, n_{Clone} is the total number of GFP+ cells in the fixed pouch, and $N_{Control}$ is the average number of contiguous control GFP+ cell population in the fixed pouch.

Statistical analyses.—Sample sizes were based on the standard of the field. While determining parameters relating to individual cells like apical cell area or cell sidedness we

examined at the minimum 300 cells from at least five different wing discs. While determining parameters relating to whole wing pouch like the total cell number or cell dispersal, we examined at least five different wing discs. In the box-plots, circles represent mean values from individual wing discs unless specified, the diamond box contains 25–75% percentiles of the data and the bar denotes the median. All statistical significance tests and curve fits were carried out using Origin (OriginLab).

Data Availability

Original data underlying this manuscript can be accessed from the Stowers Original Data Repository at http://www.stowers.org/research/publications/libpb-1374.

Supplementary Material

Refer to Web version on PubMed Central for supplementary material.

ACKNOWLEDGMENTS

We thank Boris Rubinstein, Stanislav Shvartsman, Denis Weaire, Sean McKinney and the members of the Gibson lab for discussions and advice. We thank Kendra Marr for assistance in establishing fly lines and Davide Heller for support with EpiTools. This work was supported by the Stowers Institute for Medical Research and grants from the National Institutes of Health (R01GM111733-05 to M.C.G). Original data underlying this manuscript can be accessed from the Stowers Original Data Repository at http://www.stowers.org/research/publications/libpb-1374.

REFERENCES

Anderson RS, and Bunas KL (1993). Grain size segregation and stratigraphy in aeolian ripples modelled with a cellular automaton. Nature 365, 740–743.

Barcelo H, and Stewart MJ (2002). Altering Drosophila S6 kinase activity is consistent with a role for S6 kinase in growth. Genesis 34, 83–85. [PubMed: 12324955]

Bardet P-L, Guirao B, Paoletti C, Serman F, Léopold V, Bosveld F, Goya Y, Mirouse V, Graner F, and Bellaïche Y (2013). PTEN controls junction lengthening and stability during cell rearrangement in epithelial tissue. Dev. Cell 25, 534–546. [PubMed: 23707736]

Bateman JM, and McNeill H (2004). Temporal Control of Differentiation by the Insulin Receptor/Tor Pathway in Drosophila. Cell 119, 87–96. [PubMed: 15454083]

Bertet C, Sulak L, and Lecuit T (2004). Myosin-dependent junction remodelling controls planar cell intercalation and axis elongation. Nature 429, 667–671. [PubMed: 15190355]

Bi D, Lopez JH, Schwarz JM, and Manning ML (2015). A density-independent rigidity transition in biological tissues. Nat. Phys. 11, 1074–1079.

Bosveld F, Guirao B, Wang Z, Rivière M, Bonnet I, Graner F, and Bellaïche Y (2016). Modulation of junction tension by tumor suppressors and proto-oncogenes regulates cell-cell contacts. Development 143, 623–634. [PubMed: 26811379]

Brand AH, and Perrimon N (1993). Targeted gene expression as a means of altering cell fates and generating dominant phenotypes. Development 118, 401–415. [PubMed: 8223268]

Cavallaro U, Schaffhauser B, and Christofori G (2002). Cadherins and the tumour progression: is it all in a switch? Cancer Lett. 176, 123–128. [PubMed: 11804738]

Cavey M, Rauzi M, Lenne P-F, and Lecuit T (2008). A two-tiered mechanism for stabilization and immobilization of E-cadherin. Nature 453, 751–756. [PubMed: 18480755]

Chabab S, Lescroart F, Rulands S, Mathiah N, Simons BD, and Blanpain C (2016). Uncovering the Number and Clonal Dynamics of Mesp1 Progenitors during Heart Morphogenesis. Cell Rep. 14, 1–10. [PubMed: 26725109]

Corrado F, Ferri C, Mannini D, Corrado G, Bertoni F, Bacchini P, Lelli G, Lieber MM, and Song JM (1991). Transitional Cell Carcinoma of the Upper Urinary Tract: Evaluation of Prognostic Factors by Histopathology and Flow Cytometric Analysis. J. Urol. 145, 1159–1163. [PubMed: 2033684]

Di Gregorio A, Bowling S, and Rodriguez TA (2016). Cell Competition and Its Role in the Regulation of Cell Fitness from Development to Cancer. Dev. Cell 38, 621–634. [PubMed: 27676435]

Dreher D, Pasakarnis L, and Brunner D (2016). SnapShot: Mechanical Forces in Development II. Cell 165, 1028–1028.e1. [PubMed: 27153501]

Durand M, Kraynik AM, van Swol F, Käfer J, Quilliet C, Cox S, Ataei Talebi S, and Graner F (2014). Statistical mechanics of two-dimensional shuffled foams: Geometry-topology correlation in small or large disorder limits. Phys. Rev. E 89, 062309.

El-Naggar A, Chan J, Grandis J, Takata T, and Slootweg P (2017). WHO Classification of Head and Neck Tumours (Lyon: International Agency for Research on Cancer).

Erami Z, Herrmann D, Warren SC, Nobis M, McGhee EJ, Lucas MC, Leung W, Reischmann N, Mrowinska A, Schwarz JP, et al. (2016). Intravital FRAP Imaging using an E-cadherin-GFP Mouse Reveals Disease- and Drug-Dependent Dynamic Regulation of Cell-Cell Junctions in Live Tissue. Cell Rep. 14, 152–167. [PubMed: 26725115]

Fagotto F (2014). The cellular basis of tissue separation. Development 141, 3303–3318. [PubMed: 25139853]

Farhadifar R, Röper J-C, Aigouy B, Eaton S, and Julicher F (2007). The Influence of Cell Mechanics, Cell-Cell Interactions, and Proliferation on Epithelial Packing. Curr. Biol. 17, 2095–2104. [PubMed: 18082406]

Forsberg LA, Gisselsson D, and Dumanski JP (2017). Mosaicism in health and disease - clones picking up speed. Nat. Rev. Genet. 18, 128–142. [PubMed: 27941868]

Freed D, Stevens EL, and Pevsner J (2014). Somatic Mosaicism in the Human Genome. Genes 5, 1064–1094. [PubMed: 25513881]

Gibson MC, Patel AB, Nagpal R, and Perrimon N (2006). The emergence of geometric order in proliferating metazoan epithelia. Nature 442, 1038–1041. [PubMed: 16900102]

Ginzberg MB, Kafri R, and Kirschner M (2015). On being the right (cell) size. Science 348, 1245075. [PubMed: 25977557]

Goh BKP, Chow PKH, Teo J-Y, Wong J-S, Chan C-Y, Cheow P-C, Chung AYF, and Ooi LLPJ (2014). Number of Nodules, Child-Pugh Status, Margin Positivity, and Microvascular Invasion, but not Tumor Size, are Prognostic Factors of Survival after Liver Resection for Multifocal Hepatocellular Carcinoma. J. Gastrointest. Surg. 18, 1477–1485. [PubMed: 24855028]

Gómez-Gálvez P, Vicente-Munuera P, Tagua A, Forja C, Castro AM, Letrán M, Valencia-Expósito A, Grima C, Bermúdez-Gallardo M, Serrano-Pérez-Higueras Ó, et al. (2018). Scutoids are a geometrical solution to three-dimensional packing of epithelia. Nat. Commun. 9, 2960. [PubMed: 30054479]

Graner F, and Riveline D (2017). 'The Forms of Tissues, or Cell-aggregates': D'Arcy Thompson's influence and its limits. Development 144, 4226–4237. [PubMed: 29183936]

Guirao B, and Bellaïche Y (2017). Biomechanics of cell rearrangements in Drosophila. Curr. Opin. Cell Biol. 48, 113–124. [PubMed: 28732313]

Gumbiner BM (2005). Regulation of cadherin-mediated adhesion in morphogenesis. Nat. Rev. Mol. Cell Biol. 6, 622–634. [PubMed: 16025097]

Hafner C, Knuechel R, Zanardo L, Dietmaier W, Blaszyk H, Cheville J, Hofstaedter F, and Hartmann A (2001). Evidence for oligoclonality and tumor spread by intraluminal seeding in multifocal urothelial carcinomas of the upper and lower urinary tract. Oncogene 20, 4910–4915. [PubMed: 11521204]

Heller D, Hoppe A, Restrepo S, Gatti L, Tournier AL, Tapon N, Basler K, and Mao Y (2016). EpiTools: An Open-Source Image Analysis Toolkit for Quantifying Epithelial Growth Dynamics. Dev. Cell 36, 103–116. [PubMed: 26766446]

Hennig KM, and Neufeld TP (2002). Inhibition of cellular growth and proliferation by dTOR overexpression in Drosophila. Genesis 34, 107–110. [PubMed: 12324961]

Hilgenfeldt S (2013). Size-topology correlations in disk packings: terminal bidispersity in order–disorder transitions. Philos. Mag. 93, 4018–4029.

Hoffman BD, and Crocker JC (2009). Cell Mechanics: Dissecting the Physical Responses of Cells to Force. Annu. Rev. Biomed. Eng. 11, 259–288. [PubMed: 19400709]

Hsu H-C, Chiou T-J, Chen J-Y, Lee C-S, Lee P-H, and Peng S-Y (1991). Clonality and clonal evolution of hepatocellular carcinoma with multiple nodules. Hepatology 13, 923–928. [PubMed: 1851494]

Huang J, Wu S, Barrera J, Matthews K, and Pan D (2005). The Hippo signaling pathway coordinately regulates cell proliferation and apoptosis by inactivating Yorkie, the Drosophila Homolog of YAP. Cell 122, 421–434. [PubMed: 16096061]

Huang J, Zhou W, Dong W, Watson AM, and Hong Y (2009). Directed, efficient, and versatile modifications of the Drosophila genome by genomic engineering. Proc. Natl. Acad. Sci. U. S. A. 106, 8284–8289. [PubMed: 19429710]

Hufnagel L, Teleman AA, Rouault H, Cohen SM, and Shraiman BI (2007). On the mechanism of wing size determination in fly development. Proc. Natl. Acad. Sci. 104, 3835–3840. [PubMed: 17360439]

Johnston LA, Prober DA, Edgar BA, Eisenman RN, and Gallant P (1999). Drosophila myc regulates cellular growth during development. Cell 98, 779–790. [PubMed: 10499795]

Kim S, Cai M, and Hilgenfeldt S (2014). Lewis' law revisited: the role of anisotropy in size–topology correlations. New J. Phys. 16, 015024.

Kim TY, Hong SJ, Kim JM, Gu Kim W, Gong G, Ryu JS, Kim WB, Yun S-C, and Shong YK (2008). Prognostic parameters for recurrence of papillary thyroid microcarcinoma. BMC Cancer 8, 296. [PubMed: 18851763]

Kouzak SS, Mendes MST, Costa IMC, Kouzak SS, Mendes MST, and Costa IMC (2013). Cutaneous mosaicisms: concepts, patterns and classifications. An. Bras. Dermatol. 88, 507–517. [PubMed: 24068120]

Lambertsson A (1998). 3 The Minute Genes in Drosophila and Their Molecular Functions In Advances in Genetics, Hall JC, Dunlap JC, Friedmann T, and Giannelli F, eds. (Academic Press), pp. 69–134.

Leckband D, and Prakasam A (2006). Mechanism and Dynamics of Cadherin Adhesion. Annu. Rev. Biomed. Eng. 8, 259–287. [PubMed: 16834557]

Lecuit T, and Yap AS (2015). E-cadherin junctions as active mechanical integrators in tissue dynamics. Nat. Cell Biol. 17, 533–539. [PubMed: 25925582]

Lee T, and Luo L (1999). Mosaic analysis with a repressible cell marker for studies of gene function in neuronal morphogenesis. Neuron 22, 451–461. [PubMed: 10197526]

Levayer R, Hauert B, and Moreno E (2015). Cell mixing induced by myc is required for competitive tissue invasion and destruction. Nature 524, 476–480. [PubMed: 26287461]

Lewis FT (1928). The correlation between cell division and the shapes and sizes of prismatic cells in the epidermis of cucumis. Anat. Rec. 38, 341–376.

Li W, Kale A, and Baker NE (2009). Oriented cell division as a response to cell death and cell competition. Curr. Biol. CB 19, 1821–1826. [PubMed: 19853449]

Lim ET, Uddin M, Rubeis SD, Chan Y, Kamumbu AS, Zhang X, D'Gama AM, Kim SN, Hill RS, Goldberg AP, et al. (2017). Rates, distribution and implications of postzygotic mosaic mutations in autism spectrum disorder. Nat. Neurosci. 20, 1217–1224. [PubMed: 28714951]

Lloyd AC (2013). The Regulation of Cell Size. Cell 154, 1194–1205. [PubMed: 24034244]

Lupski JR (2013). Genome Mosaicism—One Human, Multiple Genomes. Science 341, 358–359. [PubMed: 23888031]

Lutzeyer W, Rübben H, and Dahm H (1982). Prognostic Parameters in Superficial Bladder Cancer: An Analysis of 315 Cases. J. Urol. 127, 250–252. [PubMed: 7062375]

Lynch M (2010). Evolution of the mutation rate. Trends Genet. 26, 345–352. [PubMed: 20594608]

Machiela MJ, and Chanock SJ (2017). The ageing genome, clonal mosaicism and chronic disease. Curr. Opin. Genet. Dev. 42, 8–13. [PubMed: 28068559]

Marcq M, and Galy P (1973). Bronchioloalveolar Carcinoma. Am. Rev. Respir. Dis. 107, 621–629. [PubMed: 4348944]

Martin AC, Kaschube M, and Wieschaus EF (2009). Pulsed contractions of an actin-myosin network drive apical constriction. Nature 457, 495–499. [PubMed: 19029882]

McCarthy RP, Wang M, Jones TD, Strate RW, and Cheng L (2006). Molecular Evidence for the Same Clonal Origin of Multifocal Papillary Thyroid Carcinomas. Clin. Cancer Res. 12, 2414–2418. [PubMed: 16638846]

Merino MM, Rhiner C, Lopez-Gay JM, Buechel D, Hauert B, and Moreno E (2015). Elimination of unfit cells maintains tissue health and prolongs lifespan. Cell 160, 461–476. [PubMed: 25601460]

Meyer EJ, Ikmi A, and Gibson MC (2011). Interkinetic nuclear migration is a broadly conserved feature of cell division in pseudostratified epithelia. Curr. Biol. 21, 485–491. [PubMed: 21376598]

Miller GJ, and Cygan JM (1994). Morphology of Prostate Cancer: The Effects of Multifocality on Histological Grade, Tumor Volume and Capsule Penetration. J. Urol. 152, 1709–1713. [PubMed: 7933231]

Monier B, Gettings M, Gay G, Mangeat T, Schott S, Guarner A, and Suzanne M (2015). Apico-basal forces exerted by apoptotic cells drive epithelium folding. Nature 518, 245–248. [PubMed: 25607361]

Montagne J, Stewart MJ, Stocker H, Hafen E, Kozma SC, and Thomas G (1999). Drosophila S6 Kinase: A Regulator of Cell Size. Science 285, 2126–2129. [PubMed: 10497130]

Morita M, Gravel S-P, Hulea L, Larsson O, Pollak M, St-Pierre J, and Topisirovic I (2015). mTOR coordinates protein synthesis, mitochondrial activity and proliferation. Cell Cycle 14, 473–480. [PubMed: 25590164]

Munjal A, and Lecuit T (2014). Actomyosin networks and tissue morphogenesis. Development 141, 1789–1793. [PubMed: 24757001]

Nakajima Y, Meyer EJ, Kroesen A, McKinney SA, and Gibson MC (2013). Epithelial junctions maintain tissue architecture by directing planar spindle orientation. Nature 500, 359–362. [PubMed: 23873041]

Neufeld TP, de la Cruz AFA, Johnston LA, and Edgar BA (1998). Coordination of Growth and Cell Division in the Drosophila Wing. Cell 93, 1183–1193. [PubMed: 9657151]

Oldham S, Böhni R, Stocker H, Brogiolo W, and Hafen E (2000). Genetic control of size in Drosophila. Philos. Trans. R. Soc. B Biol. Sci. 355, 945–952.

Pandis N, Teixeira MR, Gerdes A-M, Limon J, Bardi G, Andersen JA, Idvall I, Mandahl N, Mitelman F, and Heim S (1995). Chromosome abnormalities in bilateral breast carcinomas. Cytogenetic evaluation of the clonal origin of multiple primary tumors. Cancer 76, 250–258. [PubMed: 8625100]

Pasakarnis L, Dreher D, and Brunner D (2016). SnapShot: Mechanical Forces in Development I. Cell 165, 754–754.e1. [PubMed: 27104981]

Porta CAML, and Zapperi S (2017). The Physics of Cancer (Cambridge University Press).

Ramanathan SP, Helenius J, Stewart MP, Cattin CJ, Hyman AA, and Muller DJ (2015). Cdk1-dependent mitotic enrichment of cortical myosin II promotes cell rounding against confinement. Nat. Cell Biol. 17, 148–159. [PubMed: 25621953]

Rauzi M, Lenne P-F, and Lecuit T (2010). Planar polarized actomyosin contractile flows control epithelial junction remodelling. Nature 468, 1110–1114. [PubMed: 21068726]

Resino J, Salama-Cohen P, and Garcia-Bellido A (2002). Determining the role of patterned cell proliferation in the shape and size of the Drosophila wing. Proc. Natl. Acad. Sci. U. S. A. 99, 7502–7507. [PubMed: 12032312]

Rosato A, Strandburg KJ, Prinz F, and Swendsen RH (1987). Why the Brazil nuts are on top: Size segregation of particulate matter by shaking. Phys. Rev. Lett. 58, 1038–1040. [PubMed: 10034316]

Ruijter ETG, Miller GJ, van de Kaa CA, van Bokhoven A, Bussemakers MJG, Debruyne FMJ, Ruiter DJ, and Schalken JA (1999). Molecular analysis of multifocal prostate cancer lesions. J. Pathol. 188, 271–277. [PubMed: 10419595]

Rulands S, Lescroart F, Chabab S, Hindley CJ, Prior N, Sznurkowska MK, Huch M, Philpott A, Blanpain C, and Simons BD (2018). Universality of clone dynamics during tissue development. Nat. Phys. 1.

Saucedo LJ, Gao X, Chiarelli DA, Li L, Pan D, and Edgar BA (2003). Rheb promotes cell growth as a component of the insulin/TOR signalling network. Nat. Cell Biol. 5, 566–571. [PubMed: 12766776]

Saw TB, Doostmohammadi A, Nier V, Kocgozlu L, Thampi S, Toyama Y, Marcq P, Lim CT, Yeomans JM, and Ladoux B (2017). Topological defects in epithelia govern cell death and extrusion. Nature 544, 212–216. [PubMed: 28406198]

Saxton RA, and Sabatini DM (2017). mTOR Signaling in Growth, Metabolism, and Disease. Cell 168, 960–976. [PubMed: 28283069]

Schmoller KM, and Skotheim JM (2015). The Biosynthetic Basis of Cell Size Control. Trends Cell Biol. 25, 793–802. [PubMed: 26573465]

Sidransky D, Frost P, Von Eschenbach A, Oyasu R, Preisinger AC, and Vogelstein B (1992). Clonal origin of bladder cancer. N. Engl. J. Med. 326, 737–740. [PubMed: 1445507]

Simpson P (1979). Parameters of cell competition in the compartments of the wing disc of Drosophila. Dev. Biol. 69, 182–193. [PubMed: 446891]

Stuelten CH, Parent CA, and Montell DJ (2018). Cell motility in cancer invasion and metastasis: insights from simple model organisms. Nat. Rev. Cancer 18, 296–312. [PubMed: 29546880]

Sun Z, Amourda C, Shagirov M, Hara Y, Saunders TE, and Toyama Y (2017). Basolateral protrusion and apical contraction cooperatively drive Drosophila germ-band extension. Nat. Cell Biol. 19, 375. [PubMed: 28346438]

Talmadge JE, and Fidler IJ (2010). AACR Centennial Series: The Biology of Cancer Metastasis: Historical Perspective. Cancer Res. 0008-5472.CAN-10–1040.

Travis WD, Brambilla B, Burke AP, Marx A, and Nicholson AG (2015). WHO Classification of Tumours of the Lung, Pleura, Thymus and Heart (Lyon: International Agency for Research on Cancer).

Tsuboi A, Ohsawa S, Umetsu D, Sando Y, Kuranaga E, Igaki T, and Fujimoto K (2018). Competition for Space Is Controlled by Apoptosis-Induced Change of Local Epithelial Topology. Curr. Biol. CB 28, 2115–2128.e5. [PubMed: 29910075]

Vachias C, Fritsch C, Pouchin P, Bardot O, and Mirouse V (2014). Tight Coordination of Growth and Differentiation between Germline and Soma Provides Robustness for Drosophila Egg Development. Cell Rep. 9, 531–541. [PubMed: 25373901]

Vanderleest TE, Smits CM, Xie Y, Jewett CE, Blankenship JT, and Loerke D (2018). Vertex sliding drives intercalation by radial coupling of adhesion and actomyosin networks during Drosophila germband extension.

Waclaw B, Bozic I, Pittman ME, Hruban RH, Vogelstein B, and Nowak MA (2015). A spatial model predicts that dispersal and cell turnover limit intratumour heterogeneity. Nature 525, 261–264. [PubMed: 26308893]

Wang T, and Edgar BA (2010). 11 - TOR Signaling and Cell Death In The Enzymes, Tamanoi F, and Hall MN, eds. (Academic Press), pp. 217–244.

Wang T, Blumhagen R, Lao U, Kuo Y, and Edgar BA (2012). LST8 Regulates Cell Growth via Target-of-Rapamycin Complex 2 (TORC2). Mol. Cell. Biol. 32, 2203–2213. [PubMed: 22493059]

Wang X, Wang M, MacLennan GT, Abdul-Karim FW, Eble JN, Jones TD, Olobatuyi F, Eisenberg R, Cummings OW, Zhang S, et al. (2009). Evidence for Common Clonal Origin of Multifocal Lung Cancers. JNCI J. Natl. Cancer Inst. 101, 560–570. [PubMed: 19351924]

Weaire D, and Rivier N (1984). Soap, cells and statistics—random patterns in two dimensions. Contemp. Phys. 25, 59–99.

Weissenbacher TM, Zschage M, Janni W, Jeschke U, Dimpfl T, Mayr D, Rack B, Schindlbeck C, Friese K, and Dian D (2010). Multicentric and multifocal versus unifocal breast cancer: is the tumor-node-metastasis classification justified? Breast Cancer Res. Treat. 122, 27–34. [PubMed: 20454925]

Williams M, Yen W, Lu X, and Sutherland A (2014). Distinct Apical and Basolateral Mechanisms Drive Planar Cell Polarity-Dependent Convergent Extension of the Mouse Neural Plate. Dev. Cell 29, 34–46. [PubMed: 24703875]

Yamada S, Pokutta S, Drees F, Weis WI, and Nelson WJ (2005). Deconstructing the Cadherin-Catenin-Actin Complex. Cell 123, 889–901. [PubMed: 16325582]

Yang Q, Inoki K, Kim E, and Guan K-L (2006a). TSC1/TSC2 and Rheb have different effects on TORC1 and TORC2 activity. Proc. Natl. Acad. Sci. U. S. A. 103, 6811–6816. [PubMed: 16627617]

Yang Q, Inoki K, Ikenoue T, and Guan K-L (2006b). Identification of Sin1 as an essential TORC2 component required for complex formation and kinase activity. Genes Dev. 20, 2820–2832. [PubMed: 17043309]

Zhang H, Stallock JP, Ng JC, Reinhard C, and Neufeld TP (2000). Regulation of cellular growth by the Drosophila target of rapamycin dTOR. Genes Dev. 14, 2712–2724. [PubMed: 11069888]

Highlights

- Growth heterogeneity induces dispersal of small cells within mosaic epithelial tissue.
- Dispersal of small cells is not due to differential activity of junctional proteins.
- Geometric effects of growth discrepancies are sufficient to disperse aberrant cells.

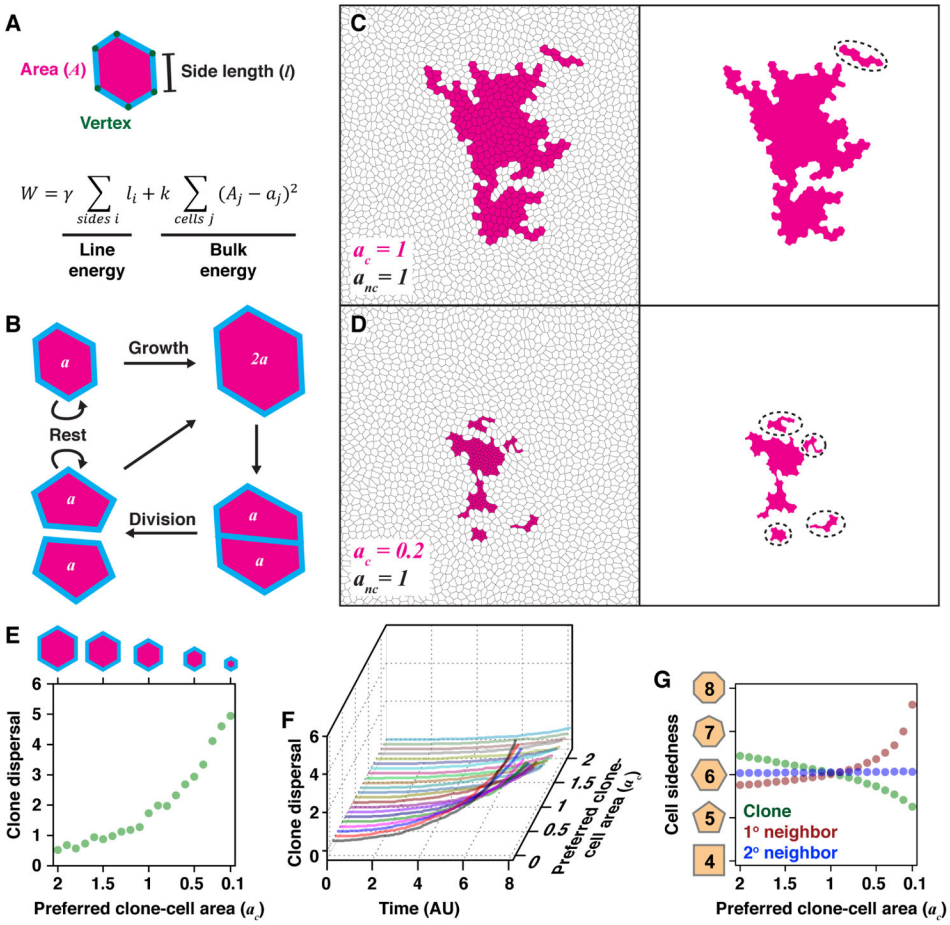

Figure 1. Small-cell clones tend to disperse *in silico*

(A) In the *in silico* model, cells are represented by polygons with straight sides (*cyan*) and parametrized by vertices (*green*). Their mechanical state is characterized by their surface areas A (*magenta*) and side lengths l (*black*). The depicted equation relates the potential energy W of the tissue to the sum of work done to acquire cell side lengths l_i and to deviate cell areas A_j from their preferred value a_j. Line-tension γ and area-compression k moduli remained constant in all simulations. During simulation, the vertices move so as to minimize the potential energy.

(B) Implementing cell growth and division in the vertex model. Cells spend the majority of time in a rest phase. Subsequently, cells enter a phase of growth when their preferred area is increased linearly with time. Cells divide when their preferred area is double the rest phase preferred area.

(C and D) Representative snapshots of mosaic tissue generated after ~8 rounds of cell division. Clonal cells (*magenta*) were derived from a single progenitor cell at the start of the simulation. The preferred clone cell area a_c was set at either 1 (C) or 0.2 (D), while the preferred area of non-clone cells a_{nc} was set at 1. All cells had the same division rate and featured random orientation of cleavage. Instances of dispersal are circled with dashed lines.

(E) Clone cell dispersal after ~8 rounds of cell division over a range of preferred clone cell areas between 0.1 and 2, while that of non-clone cells was 1. Clone cell dispersal is the

number of instances where non-clone neighbors intervene clonal cell population. For each preferred cell area, the simulation was repeated 200 times.

(F) The temporal dynamics of clone cell dispersal over a range of preferred clone cell areas between 0.1 and 2.

(G) Cell sidedness after ~8 rounds of cell division. Clonal cells at the non-clone interface are denoted with *green*, their immediate non-clone 1º neighbors with *brown* and their 2º neighbors with *blue*.

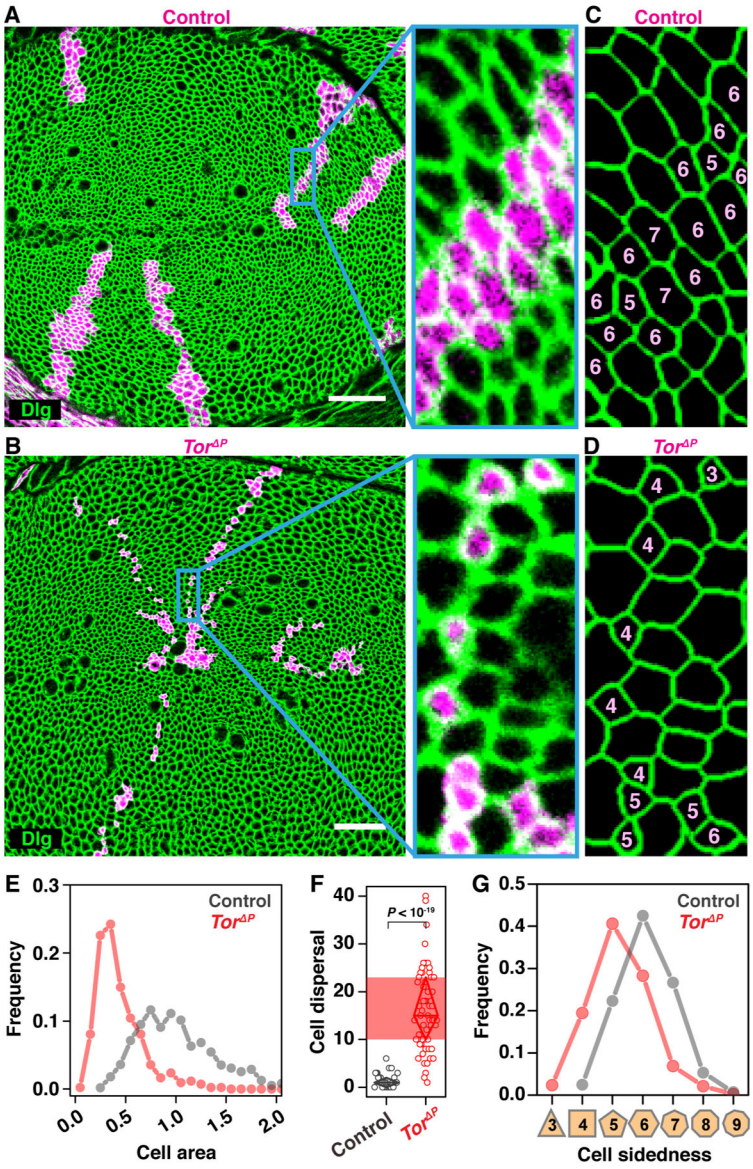

Figure 2. *Tor*$^{\Delta P}$ clones are frequently interposed by larger neighboring cells

(A and B) *FRT40A* control (A, $n = 29$ wing discs) and *Tor*$^{\Delta P}$ (B, $n = 62$ wing discs) cell clones expressing GFP (*magenta*) and stained for Dlg (*green*) to visualize junctions in wing disc epithelia. Scale bars, 20 μm.

(C and D) Skeletonized junctions with cell-sidedness inscribed within the clonal *FRT40A* control (C) and *Tor*$^{\Delta P}$ (D) cells.

(E) The frequency distribution of relative area in *FRT40A* control (*grey,* $n = 937$ cells) and *Tor*$^{\Delta P}$ cells (*red,* $n = 421$ cells).

(F) Cell dispersal in *FRT40A* control ($n = 28$ wing discs) and *Tor*$^{\Delta P}$ ($n = 52$ wing discs) clones. Clone cell dispersal is the number of instances wherein mutant cells (*magenta*) were intervened by exactly one non-mutant neighbor in the wing pouch. Unless otherwise specified, in this and every following box-plot, circles represent mean values from individual

wing discs, the diamond box contains 25–75% percentiles of the data and the bar denotes the median. *P*-value, unpaired two-sample *t*-test.

(G) The frequency distribution of sidedness in *FRT40A* control (*grey, n* = 937 cells) and $Tor^{\Delta P}$ cells (*red, n* = 421 cells).

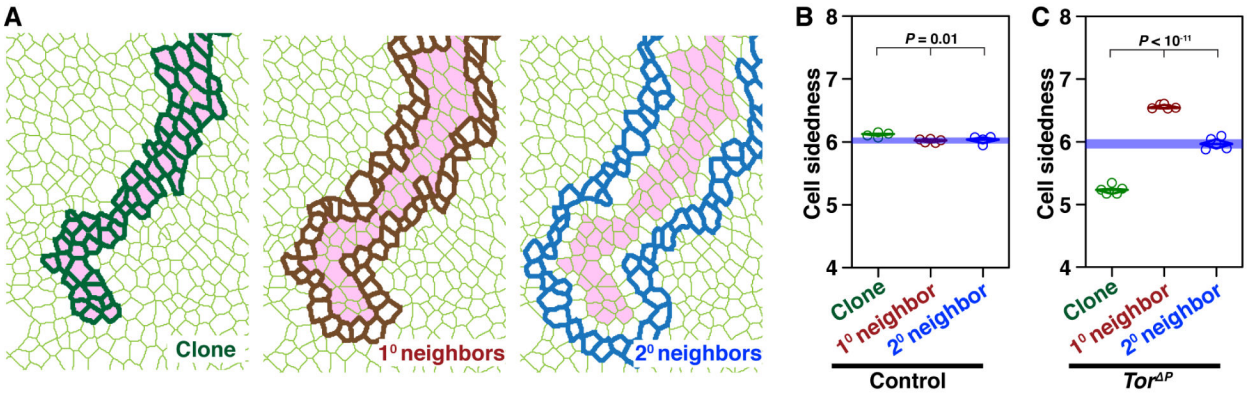

Figure 3. *Tor*$^{\Delta P}$ cells lose sides to their larger neighbors

(A) Illustration of a cell clone (*dark green*) and its non-clone 1^0 and 2^0 neighbors (*brown* and *blue*, respectively).

(B and C) Cell sidedness of *FRT40A* control clones (B, $n = 937$ cells) and *Tor*$^{\Delta P}$ clones (c, $n = 421$ cells) along with their 1^0 and 2^0 neighbor cells. While *Tor*$^{\Delta P}$ cells tend to lose sides, their immediate 1^0 neighbors tend to gain sides. *P*-values, one-way ANOVA.

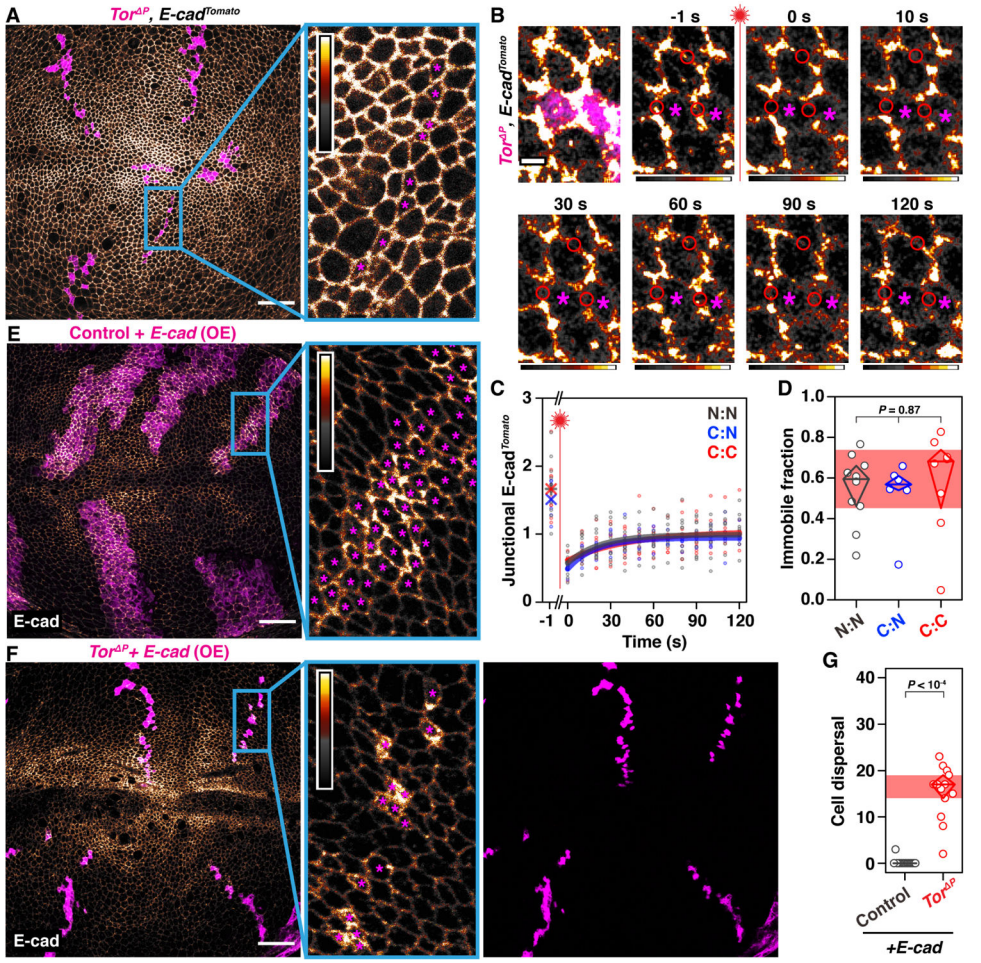

Figure 4. E-cadherin overexpression does not rescue *Tor*$^{\Delta P}$ clone dispersal

(A) *Tor*$^{\Delta P}$ clones (*magenta*, cells marked with asterisks) in the wing pouch expressing endogenous E-cadherin fused to tdTomato (n = 12 wing discs). The range of tdTomato fluorescent intensities is indicated by the calibration bar. Scale bar, 20 μm.

(B) Fluorescence recovery of junctional E-cad^{Tomato} after photobleaching (FRAP) three regions of interest (red circles) simultaneously, at −0.5 s. Clonal *Tor*$^{\Delta P}$ cells (*magenta*) are marked with asterisks. The red circles (ROIs) are on junctions shared between nonclonal (N:N), clonal-nonclonal (C:N) or clonal (C:C) cells. Scale bar, 2 μm.

(C) FRAP in N:N (grey, n = 10 ROIs, from 6 wing discs), C:N (blue, n = 6 ROIs, from 5 wing discs) and C:C (red, n = 8 ROIs, from 5 wing discs) junctions. The dots represent junctional E-cad^{Tomato} enrichment, determined by normalizing the mean pixel intensity of an ROI to that of the entire field of view. The average prebleach enrichment in each of the three junction types (at −1 s) and the corresponding postbleach recovery fits (≥ 0 s) are denoted by crosses and solid curves, respectively.

(D) The immobile fraction of junctional E-cad^{Tomato}. F-value, one-way ANOVA.

(E, F) *FRT40A* control (E, n = 15 wing discs) and *Tor*$^{\Delta P}$ (F, n = 13 wing discs) clones overexpressing E-cad and GFP (*magenta*, cells marked with asterisks). The range of E-cad immunostaining fluorescent intensities is indicated by the calibration bar. Scale bars, 20 μm.

(G) Cell dispersal in *FRT40A* control and $Tor^{\Delta P}$ clones overexpressing E-cad. *P*-value, unpaired two-sample *t*-test.

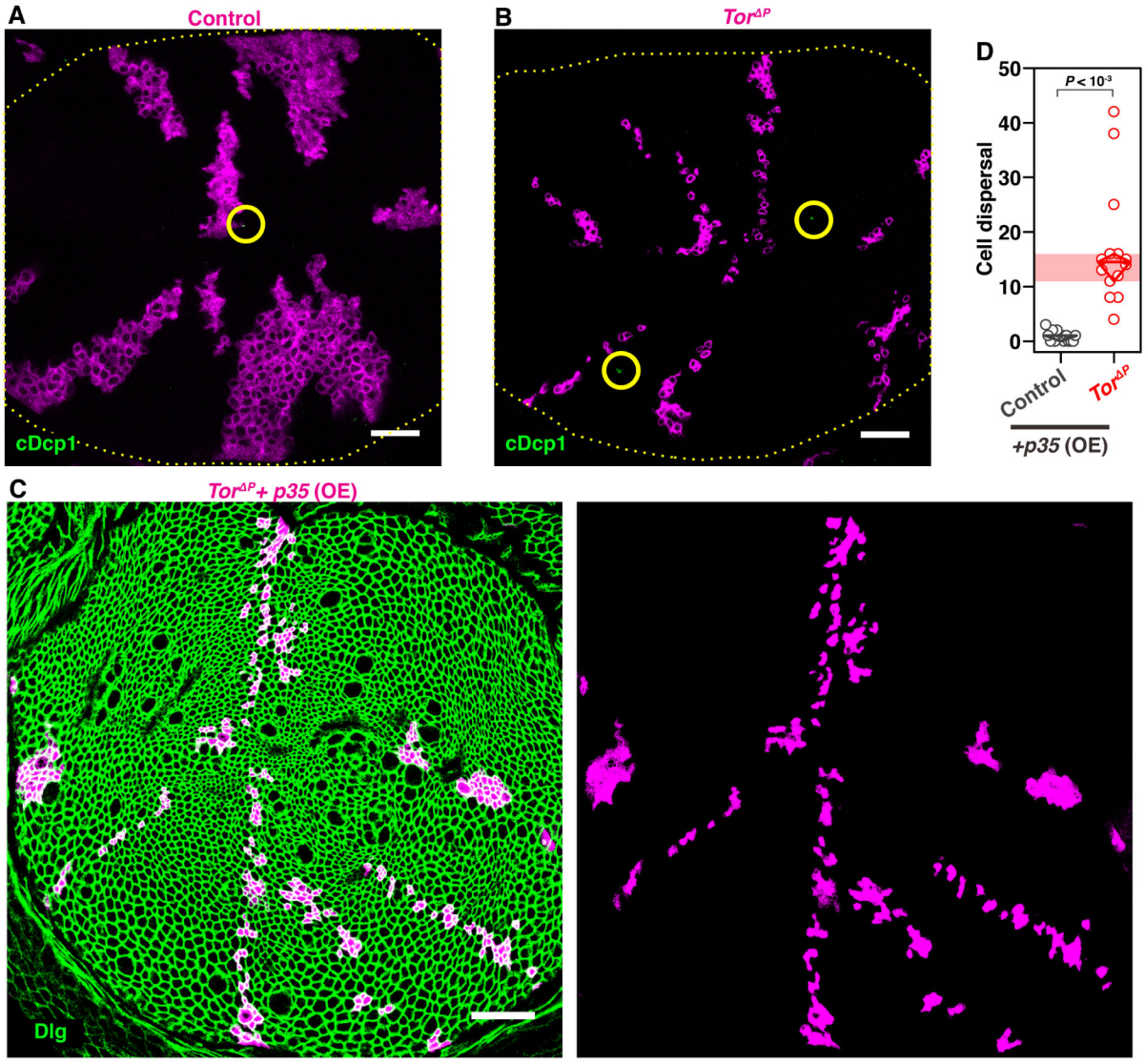

Figure 5. Apoptosis does not have a causal role in dispersing clonal *Tor*$^{\Delta P}$ cells

(A and B) *FRT40A* control (A, *n* = 5 wing discs) and *Tor*$^{\Delta P}$ (B, *n* = 6 wing discs) clones expressing GFP (*magenta*) and stained for cDcp1 (*green*) to mark apoptotic cells. Yellow dotted perimeter and circles indicate the wing disc pouch region and cDcp1 + cells, respectively.

(C) *Tor*$^{\Delta P}$ clones that overexpress the cell-death repressor p35 and GFP (*magenta*).

(D) Cell dispersal in *FRT40A* control (*n* = 14 wing discs) and *Tor*$^{\Delta P}$ (*n* = 14 wing discs) clones overexpressing the caspase inhibitor p35. *P*-value, unpaired two-sample *t*-test. Scale bars, 20 μm.

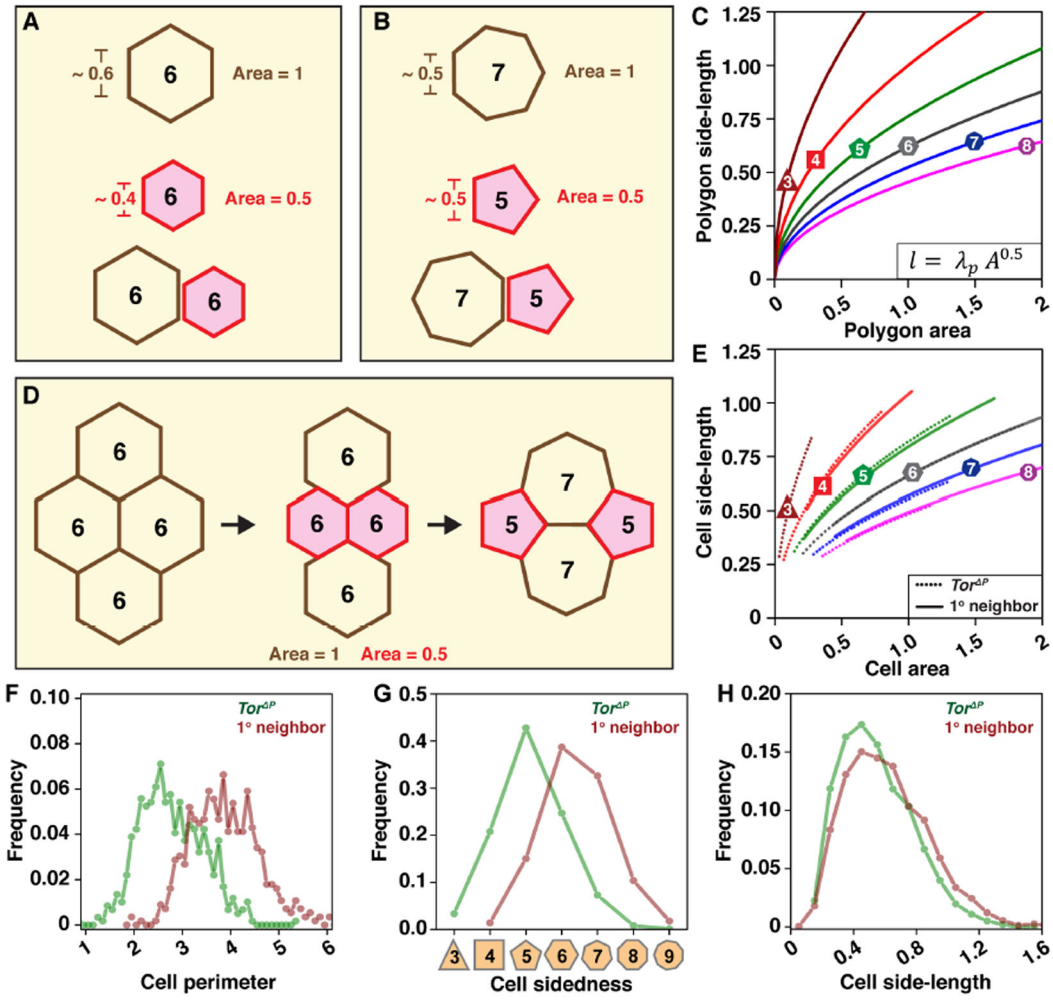

Figure 6. Smaller cells can match side-lengths with their neighbors by decreasing sidedness

(A) The side-lengths of regular hexagons with areas 1 (brown) and 0.5 (red) are mismatched.

(B) The side-lengths of regular heptagons with areas 1 and that of pentagons with 0.5 are comparable.

(C) The equation in the inset relates the side-length l of a regular polygon to its area A. The value of the coefficient λ depends on polygon sidedness p. The side-lengths of regular polygons are plotted against area for indicated polygon classes.

(D) Optimal tiling for regular polygons with mismatched areas.

(E) The square root function fits relating side-lengths and areas of epithelial cells from the wing disc for cells in the indicated polygon categories. $Tor^{\Delta P}$ cells (n = 591 cells) and their 1^0 neighbors (n = 558 cells) are represented by dotted and solid curves, respectively. In agreement with geometric considerations, relative cell side-lengths tend to negatively correlate with cell-sidedness for a given relative apical area for both $Tor^{\Delta P}$ clones and their 1^0 neighbors.

(F-H) The frequency distribution of relative cell perimeters (F), sidedness (G) and relative side-lengths (H) for $Tor^{\Delta P}$ clones (*green,* n = 591 cells) and their 1^0 neighbors (*brown,* n = 558 cells).

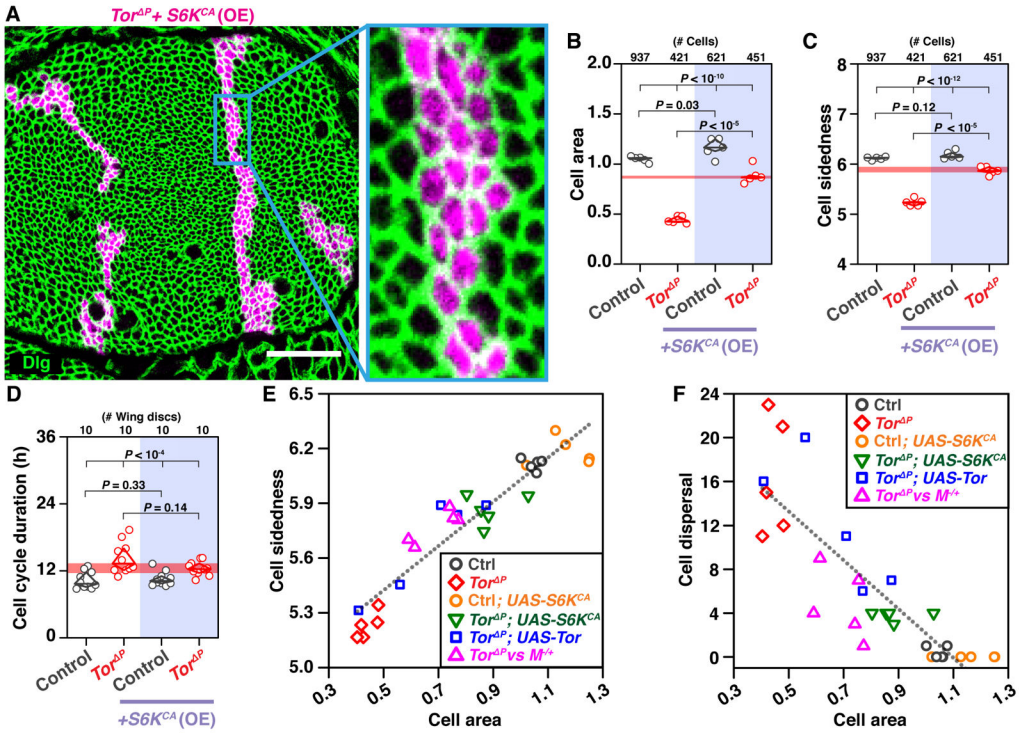

Figure 7. Reducing the size discrepancy between *Tor*$^{\Delta P}$ cells and their neighbors restores clone contiguity

(A) *Tor*$^{\Delta P}$ clones co-expressing a constitutively active version of S6 kinase (*S6K*^{CA}) and GFP (*magenta*) stained for Dlg (n = 26 wing discs). Scale bar, 20 μm.

(B, C, and D) Normalized cell area (B), cell sidedness (C) and cell cycle duration (D) of *FRT40A* control (*grey*) or *Tor*$^{\Delta P}$ (*red*) clones with and without S6K^{CA} overexpression. *P*-values, one-way ANOVA.

(E and F) Cell sidedness (E) and dispersal (F) of clonal cells plotted against their cell area. Each data point is the mean value from a wing disc containing clonal *FRT40A* control cells (*grey, n* = 937 cells), *Tor*$^{\Delta P}$ cells (*red, n* = 421 cells), *FRT40A* control cells with S6K^{CA} overexpression (*orange, n* = 621 cells), *Tor*$^{\Delta P}$ cells with S6K^{CA} overexpression (*green, n* = 451 cells) or *Tor*$^{\Delta P}$ cells with Tor overexpression (*blue, n* = 394 cells). Magenta triangles represent data from wing discs containing clonal *Tor*$^{\Delta P}$ cells surrounded by *M*$^{-/+}$ cells (n = 605 cells). The dotted line is a linear fit of the data.

KEY RESOURCES TABLE

REAGENT or RESOURCE	SOURCE	IDENTIFIER
Antibodies		
Mouse anti-*Drosophila* discs large	DSHB	4F3 anti-discs large
Rabbit anti-*Drosophila* Cleaved Dcp-1 (Asp216)	Cell signaling	#9578
Rat anti-*Drosophila* DE-cadherin	DSHB	DCAD2
Mouse anti-*Drosophila* β-catenin	DSHB	N2 7A1 Armadillo
Rabbit anti-human Phospho-Myosin Light Chain 2 (Ser19)	Cell signaling	#3671
Goat anti-mouse Alexa Fluor 647	ThermoFisher	A-21235
Goat anti-Rabbit Alexa Fluor 647	ThermoFisher	A-21244
Goat anti-Rat Alexa Fluor 647	ThermoFisher	A-21247
Goat anti-Mouse 405	ThermoFisher	A-31553
Goat anti Rabbit 405	ThermoFisher	A-31556
Experimental Models: *Drosophila melanogaster* strains		
hs-flp,UAS-GFP; Tub-Gal80, FRT40A; Tub-Gal4/TM6C	Lee and Luo, 1999	NA
w; FRT40A	BDSC	Stock # 1646
y,w,Tor$^{\Delta p}$,FRT40A/Cyo	BDSC	Stock # 7014
hs-flp,Tub-Gal4,UAS-dsRednls; Tub-Gal80,FRT40A	Guo et al., 2013	
w1118; ATPase-Alpha:GFP(trap)/TM3 ser	BDSC	Stock # 6834
UAS-mCD8:RFP	BDSC	Stock # 27392
FRT82B	BDSC	Stock # 2035
y,w; FRT82B,RheB^{2d1}/TM6B	Bateman and McNeill, 2004	NA
hs-flp,UAS-mCD8:GFP; Tub-Gal4,FRT82B,Tub-Gal80/TM6B	Nakajima et al., 2013	NA
Lst8^{1},FRT19A	Wang et al., 2012	NA
hs-flp,FRT19A,tubP-Gal80/FM7w;; UAS-mCD8:GFP,tub-Gal4/TM6B	Lee and Luo, 1999	NA
FRT42D,Sin1^{e3756}/CyO	Vachias et al., 2014	NA
UAS-CD8:GFP,hs-flp; FRT42D,tub-Gal80; tub-Gal4/TM6B	Lee et al., 2011	NA
UAS-p35	BDSC	Stock # 5073
UAS-S6K^{CA}	BDSC	Stock # 6914
UAS-Tor	BDSC	Stock # 7012
y,w,hs-flp; ubi-GFP,M(2)25A,FRT40A/CyO	Morata & Ripoll, 1975	NA
w,hs-flp; Act5C>>Gal4,UAS-GFP; UAS-Dicer2	Liang et al., 2014	NA
w,hs-flp; Act5C>>Gal4,UAS-GFP; UAS-p35	Liang et al., 2014	NA
Oregon-R	Lindsley and Grell, 1968	NA
UAS-Yorkie RNAi	BDSC	Stock # 34067
UAS-Myc RNAi	BDSC	Stock # 25783
UAS-Tor RNAi	BDSC	Stock # 34639
UAS-Rbf	BDSC	Stock # 50747

REAGENT or RESOURCE	SOURCE	IDENTIFIER
UAS-Shg	BDSC	Stock # 65589
TI{TI}Shg^{mTomato}	BDSC	Stock # 58789
Other		
F-actin stain, SiR-Jasplakinolide	Cytoskeleton	CY-SC001
SlowFade Diamond Antifade	ThermoFisher	S36963
Paraformaldehyde	Electron microscopy services	15710
TritonX-100	Sigma	T8787
Bovine insulin	Sigma	10516
Pen-Strep	Thermo Fisher Scientific	15070063
Dishwashing Liquid	Dawn	(commercially available)
0.75 mm thick glass spacers	VWR	48366227
25×75 mm glass slides	Thermo Fisher Scientific	3050
Web camera	Logitech	C920 HD Pro
Software and Algorithms		
FIJI	Schindelin, J. et al. (2012)	https://fiji.sc/
Origin	OriginLab	https://www.originlab.com/
EpiTools	Heller D. et al. (2016)	http://imls-bg-arthemis.uzh.ch/epitools-wiki/site/home/
Icy	F. de Chaumont, S et al. (2012)	http://icy.bioimageanalysis.org/
Imaris	Bitplane	http://www.bitplane.com/download
Illustrator CC	Adobe	https://www.adobe.com/